The Astronomical Journal, 135:1050–1056, 2008 March doi:10.1088/0004-6256/135/3/1050

GALAXY COUNTS AT 24 μm IN THE SWIRE FIELDS

David L. Shupe[1,2], Michael Rowan-Robinson[3], Carol J. Lonsdale[2,4], Frank Masci[1,2], Tracey Evans[2], Fan Fang[1,2], Sebastian Oliver[5], Mattia Vaccari[3,6], Giulia Rodighiero[6], Deborah Padgett[1], Jason A. Surace[1,2], C. Kevin Xu[2], Stefano Berta[4,6], Francesca Pozzi[7], Alberto Franceschini[6], Thomas Babbedge[3], Eduardo Gonzales-Solares[8], Brian D. Siana[1], Duncan Farrah[9], David T. Frayer[1,2], H. E. Smith[4], Maria Polletta[4,10], Frazer Owen[11], and Ismael Pérez-Fournon[12]

[1] Spitzer Science Center, California Institute of Technology, 314-6, Pasadena, CA 91125, USA
[2] Infrared Processing and Analysis Center, California Institute of Technology, 100-22, Pasadena, CA 91125, USA
[3] Astrophysics Group, Blackett Laboratory, Imperial College London, Prince Consort Road, London SW7 2BW, UK
[4] Center for Astrophysics and Space Sciences, University of California, San Diego, La Jolla, CA 92093-0424, USA
[5] Astronomy Centre, Department of Physics & Astronomy, University of Sussex, Brighton BN1 9QH, UK
[6] Dipartimento di Astronomia, Universita di Padova, Vicolo Osservatorio 5, I-35122 Padua, Italy
[7] Istituto Nazionale di Astrofisica, Osservatorio Astronomico di Bologna, via Ranzani 1, I-40127 Bologna, Italy
[8] Institute of Astronomy, Madingley Road, Cambridge CB3 0HA, UK
[9] Department of Astronomy, Cornell University, Space Sciences Building, Ithaca, NY 14853, USA
[10] Institut d'Astrophysique de Paris, 98bis, bd Arago-75014 Paris, France
[11] National Radio Astronomy Observatory, Socorro, NM 87801, USA
[12] Instituto Astrofiscia de Canarias, Via Lactea, 38200 La Laguna, S/C de Tenerife, Spain
Received 2006 June 27; accepted 2007 November 3; published 2008 February 14

ABSTRACT

This paper presents galaxy source counts at 24 μm in the six *Spitzer* Wide-field InfraRed Extragalactic (SWIRE) fields. The source counts are compared to counts in other fields, and to model predictions that have been updated since the launch of *Spitzer*. This analysis confirms a very steep rise in the Euclidean-normalized differential number counts between 2 mJy and 0.3 mJy. Variations in the counts between fields show the effects of sample variance in the flux range of 0.5–10 mJy, up to 100% larger than Poisson errors. Nonetheless, a "shoulder" in the normalized counts persists at around 3 mJy. The peak of the normalized counts at 0.3 mJy is higher and narrower than most models predict. In the ELAIS N1 field, the 24 μm data are combined with *Spitzer*–IRAC data and five-band optical imaging, and these band-merged data are fit with photometric redshift templates. Above 1 mJy the counts are dominated by galaxies at $z < 0.3$. By 300 μJy, about 25% are between $z \sim 0.3$ and 0.8, and a significant fraction are at $z \sim 1.3$–2. At low redshifts the counts are dominated by spirals, and starbursts rise in number density to outnumber the spirals' contribution to the counts below 1 mJy.

Key words: cosmology: observations – galaxies: evolution – galaxies: starburst – infrared: galaxies – stars: formation

Online-only material: color figures

1. INTRODUCTION

Galaxy counts from the *Infrared Astronomical Satellite* (*IRAS*) first hinted at strong evolution of luminous infrared galaxies (Hacking et al. 1987; Lonsdale & Chokshi 1993; Gregorich et al. 1995). Mid-infrared surveys made with the ISOCAM instrument at 15 microns revealed an excess population at $z \sim 0.8$ (Elbaz et al. 1999, 2002; Franceschini et al. 2001). This population was detected in part by the redshifting of the strong 7.7 micron polycyclic aromatic hydrocarbon (PAH) feature into the 15 μm band.

The high sensitivity at 24 μm of the MIPS instrument (Rieke et al. 2004) onboard *Spitzer* allows infrared-luminous galaxies to be traced to even higher redshifts. Sensitivity to obscured starbursts at $z \sim 2$ is enhanced due to redshifting of the 7.7 micron feature into the 24 μm band. First source counts have been presented by Chary et al. (2004) for the deep Great Observatory Origins Deep Survey (GOODS) test field, by Marleau et al. (2004) for the First-Look Survey (FLS) and the GOODS test field, and by Papovich et al. (2004) for a range of Guaranteed Time Observer (GTO) fields plus the GOODS test field. These counts show a steep bump in the normalized source counts as fluxes decrease from several mJy to about 300 μJy, that is attributed to the population discovered by ISOCAM at $z \sim 0.8$ plus a previously unseen population of galaxies at $z \sim 1$–2. At still fainter fluxes, the normalized counts drop off to the *Spitzer* confusion limit (Rodighiero et al. 2006; Chary et al. 2004; Marleau et al. 2004; Papovich et al. 2004).

This paper presents a detailed analysis of 24 μm source counts from the large fields observed for the *Spitzer* Wide-area InfraRed Extragalactic (SWIRE) program. The SWIRE survey is the largest of the extragalactic *Spitzer* Legacy Science programs, comprising mapping of 49 deg^2 at a wavelength from 3.6 to 160 μm (Lonsdale et al. 2003, 2004). This survey is designed to dramatically improve our understanding of galaxy evolution, including the history of star formation, the assembly of stellar mass in galaxies, the nature and impact of accretion processes in active nuclei, and the influence of environment on these processes at angular scales up to 3 deg (such as the study of clustering of ultraluminous infrared galaxies by Farrah et al. 2006). The SWIRE dataset encompasses six fields and so is an excellent resource for quantifying the effects of sample variance.

The goal of this paper is to present accurate *Spitzer* 24 μm counts in the flux ranging from 50 mJy to ~300 μJy. A detailed model-based interpretation of the counts is beyond the scope of this paper. However, the composition of the counts is explored for the ELAIS N1 field using the IRAC data at 3.6–8 μm (Surace et al. 2007, in preparation) as well as high-quality optical

Table 1
Area and Photometric Uncertainty for Each Field

Field	Size (deg × deg)	Area (deg^2)	σ (μJy)
ELAIS N1	3.1 × 3.0	9.64	38.8
ELAIS N2	1.9 × 2.5	4.87	37.6
Lockman	3.7 × 3.0	11.03	41.8
CDFS	2.6 × 3.0	7.67	38.5
XMM-LSS	3.1 × 3.0	8.34	48.2
ELAIS S1	2.3 × 3.0	7.03	51.2

imaging. This merged dataset provides insights into galaxy spectral energy distributions (SEDs) and populations (Rowan-Robinson et al. 2005; Polletta et al. 2007, in preparation), and is used in this paper to break down the 24 μm source counts by population and redshift.

The paper is organized as follows: the SWIRE observations and data processing are described in Section 2. The derivation and validation of source counts are presented in Section 3. Comparison with models, including recent models updated using *Spitzer* counts, is in Section 4. For the ELAIS N1 field, optical identifications, photometric redshifts, and template fitting lead to source counts subdivided by redshift and galaxy type in Section 5.

2. SWIRE 24 μm OBSERVATIONS AND DATA PROCESSING

2.1. Observations

The *Spitzer* mapping observations of the six SWIRE fields were carried out between 2003 December and 2004 December. For the mapping at 24, 70, and 160 μm, the following observing strategy using the MIPS instrument (Rieke et al. 2004) was implemented. The MIPS Scan Map Astronomical Observing Template was used with a medium scan rate. The spacing between scan legs was 148 arcsec, approximately half of the width of the $5' \times 5'$ field of view (FOV) of the 24 μm detector array. Three-degree-long scan legs were used for most Astronomical Observing Requests (AORs). Five scan legs were typically used per AOR, resulting in a cross-scan size of about $25'$. The AORs were arranged into two coverage sets, separated by half of a field of view (FOV) in the cross-scan direction. Adjacent AORs within a coverage set were overlapped sufficiently to ensure no gaps in the coverage of the 70 μm array. The approximate dimensions of the maps are given in Table 1.

With this observation layout, the typical coverage per point is 44 Basic Calibrated Data (BCD) images, each with an exposure time of 4 s, for a total of 160 s of integration time per point at 24 μm, 80 s per point at 70 μm, and 16 s per point at 160 μm. Overlap between rotated scans yielded a higher coverage in portions of each map.

Some regions received different coverage levels than described above. A 0.5 deg^2 region of the Lockman field was observed as part of Legacy validation operations, resulting in a total integration time about 1.5 times the nominal ones described above. In the Lockman and CDFS fields, the 24 μm maps include regions of higher coverage around the Guaranteed Time Observation (GTO) fields, where scans were initially embargoed. The ELAIS S1 field received only one coverage, and consequently half the nominal observing time per point, due to observing time constraints. Part of the ELAIS N1 field, which was missed in 2005 January due to an observatory standby event, was filled in 2005 July, leading to some irregularities in field shape and coverage. We have accounted for these modest differences in our analysis. Deeper GTO data within the SWIRE fields have only been used for checking the validity of our data.

2.2. Data Processing

The 24 μm raw data were processed by the S10.5 version of the Spitzer Science Center (SSC) pipelines. The flat-field images used were made separately for each scan mirror position, using SWIRE scan map data. The SWIRE processing began with the BCD images. For all fields, to even out variations in the background, the median of all the pixels in each image was subtracted from each pixel in that image. In the XMM-LSS field, removal of dark-latent artifacts was necessary, owing to the proximity of the very bright source Mira to the MIPS mapping region. For each scan leg, a self-calibration flat image was produced from the median of all uncorrected BCDs in that leg, and was normalized and divided into those BCDs before the background-subtraction step. This technique was successful because the intensity of these latents did not change appreciably over the 30 min duration of each scan leg.

To make maps, the corrected BCDs were co-added into large mosaics, using the SSC's MOPEX software (Makovoz & Marleau 2005). The mosaics were all made with $1.2''$ pixels. Cosmic rays were removed using multi-frame outlier rejection with a threshold of 2.5σ.

Source extraction was performed on the mosaic using SExtractor (Bertin & Arnout 1996). A local background of size 128×128 pixels was computed for the maps, and all the noise calculations were weighted by the inverse square of the coverage map. Photometry was output as measured in several apertures and by various extended source techniques. For the present study, we used photometry in a $5.25''$ radius aperture for point sources, and the Kron flux (Kron 1980) for extended sources. Aperture corrections were computed from comparing smaller apertures to a 30.6 arcsec diameter aperture. Then, an additional correction of 1.15 was applied to both aperture and Kron fluxes, to match the procedure used by the SSC pipelines. This additional factor is derived from the fraction of light outside the $30.6''$ aperture in theoretical TinyTim models of the point-spread function. The resulting overall correction for the $5.25''$ aperture is 1.78.

The calibration supplied with the data assumes a source spectrum of a 10,000 K blackbody (MIPS Data Handbook 2006). Galaxies detected at 24 μm generally have an SED slope of $F_\nu \sim \nu^{-1}$ or redder (Rowan-Robinson et al. 2005). Accordingly, we have color corrected our photometry to an assumed source spectrum of $F_\nu \sim \nu^{-1}$ by dividing by a factor of 0.961. Additionally, we have multiplied by a factor of 1.018 to account for a small change in the 24 μm calibration factor made in 2005 December (MIPS Data Handbook 2006).

For this work, sources are assigned the Kron flux if the SExtractor ISO_AREA value is at least 100 pixels, and the stellarity is less than 0.8. All other sources are considered point sources, and the $5.25''$ radius aperture measurement is used.

2.3. Data Quality Assessment

Estimating photometric uncertainties for extractions from mosaicked images is complicated by correlations

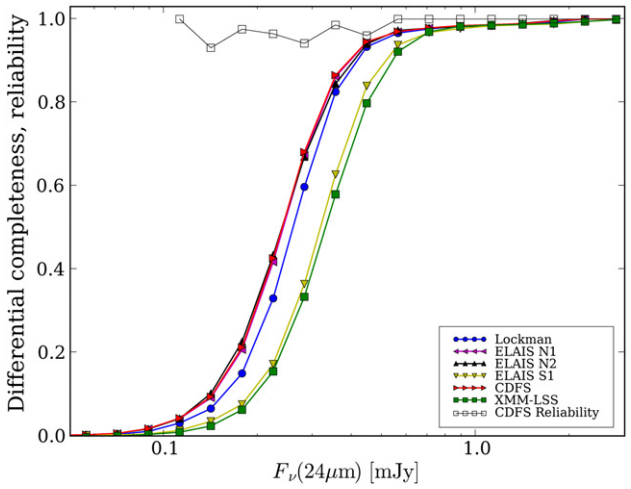

Figure 1. Filled symbols: differential completeness from simulations for ELAIS N1, ELAIS N2, and XMM-LSS fields. The curves for the other three fields were obtained by shifting the EN1 curve as described in the text. Open squares: differential reliability defined as the fraction of SWIRE sources found in the deeper GTO data in CDFS.

(A color version of this figure is available in the online journal)

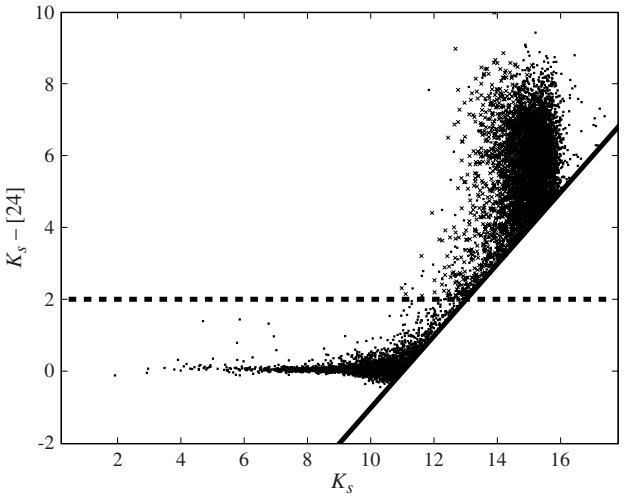

Figure 2. Color–magnitude diagram of 2MASS K_s and [24] for all six SWIRE fields. Sources with an entry in the 2MASS Extended Source Catalog are depicted by the small cross symbols. The dashed line shows the color cut used to separate out the stellar contribution (below the line) to the 24 μm number counts. The solid line depicts a 24 μm flux density limit of 300 μJy.

between pixels. To estimate the uncertainty in each field, we measured fluxes in thousands of randomly placed apertures that fell in regions of typical coverage. Gaussians were fit to the distribution of fluxes in these apertures, yielding robust uncertainty estimates. The photometric uncertainties in the 5.25″ aperture are given in Table 1. The areas in each field used in this work are also given. The relatively high noise value for the XMM-LSS field is due to its low ecliptic latitude, leading to a high zodiacal background relative to the other SWIRE fields. The noise in ELAIS S1 is higher because this field received half the integration time of the other fields.

We have estimated completeness by inserting simulated sources into the ELAIS N1, ELAIS N2, and XMM-LSS fields, and computing the fractions that are recovered. The completeness curve shifts to higher fluxes for XMM-LSS, approximately following the ratio of noise levels in Table 1. We have accordingly shifted the ELAIS N1 curve by the ratio of noise levels to estimate completeness in Lockman, ELAIS S1, and CDFS (Figure 1).

In the best fields, 70% completeness is attained for flux densities above 0.35 mJy. Based on the noise estimates in Table 1, this flux density corresponds to a signal-to-noise ratio (S/N) of about 7. Ordinarily the completeness would be expected to be higher at this S/N, but in our case the SExtractor detection parameters used have limited the completeness more than the noise has.

A direct estimate of completeness may be made by comparing the SWIRE data with deeper data. We have made such a comparison by processing GTO data in the CDFS field using the same methods used for the SWIRE data, and matching the extractions with a 3.6″ search radius. The completeness obtained from this comparison is in good agreement with the simulation results.

The comparison to deeper data is also useful as an assessment of reliability. The ratio of all matched sources to all extracted SWIRE sources is also plotted in Figure 1. The reliability defined in this way is better than 98% in all bins down to 0.35 mJy.

3. SWIRE NUMBER COUNTS

Although the contribution of stars to the 24 μm number counts is small at faint (sub-mJy) fluxes (Marleau et al. 2004; Papovich et al. 2004), it must be taken into account at fluxes of several mJy and brighter. We have used Two Micron All Sky Survey (2MASS) data to identify stars. Our 24 μm extractions were matched against the 2MASS catalog using a 3″ search radius. The resulting $K_s - [24]$ color–magnitude diagram is shown in Figure 2. [24] is the 24 μm magnitude, where we have used a zero point of 7.43 Jy in our color-corrected flux units (corresponding to 7.14 Jy for a 10,000 K blackbody spectrum, see MIPS Data Handbook 2006). The limit of 300 μJy used for our number counts corresponds to $[24] = 11.0$, well above the 2MASS completeness limit in unconfused sky of $K_s \sim 14.3$ (Skrutskie et al. 2006), and shown by the solid line in the figure. For our high Galactic latitude fields, the 2MASS survey is sensitive enough to detect all stars in the SWIRE 24 μm catalogs. The dashed line in the figure shows the simple color cut of $K_s - [24] < 2.0$ used to exclude stars for the purpose of this statistical study. A similar color discriminant method was used by Vaccari et al. (2005) with ISO 15 μm fluxes. Our color cut excludes all the 2MASS Extended Source Catalog sources that matched with the SWIRE 24 μm sources (indicated by the crosses in the figure).

Integral counts for the stars and galaxies are shown in Figure 3. The integral counts here are the total in each field, without normalization by the areas in Table 1. The contribution of stars and galaxies to the number counts is approximately equal at 30 mJy.

Euclidean-normalized number counts were obtained by computing differential counts with each source individually weighted by a factor of flux raised to the power 2.5. We have plotted these counts for all fields in Figure 4. A completeness correction has been applied for each field, using the curves shown in Figure 1, shifted for each source by the square root of the ratio of the coverage to the mean coverage. Where the completeness correction becomes large, as in the faintest bin shown for ELAIS S1, the counts are under-corrected.

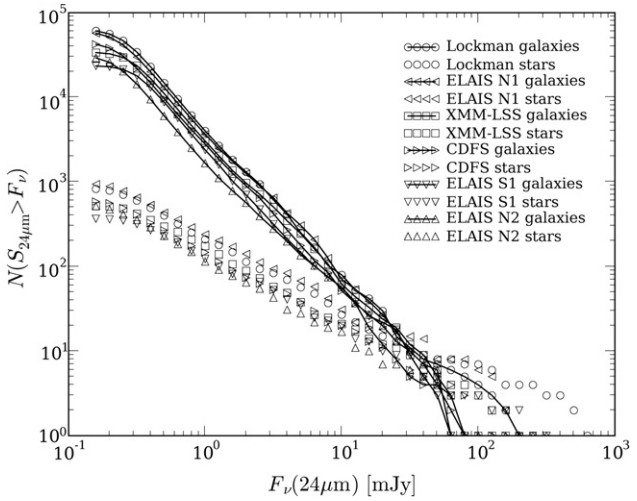

Figure 3. Integral counts for the contiguous regions in each SWIRE field. Galaxy counts are the symbols connected by lines, while stellar counts are unconnected. Note that the counts have not been normalized by area so as to provide some separation between the distributions.

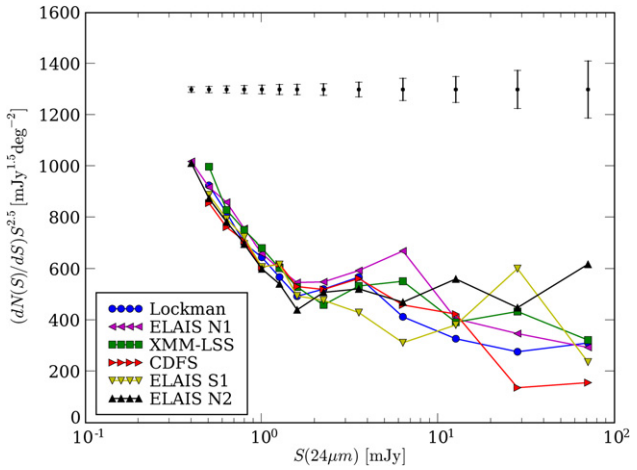

Figure 4. Normalized differential number counts for the six SWIRE fields. For clarity, representative Poisson error bars are shown at the top as computed for the ELAIS N1 field.

(A color version of this figure is available in the online journal)

The field-to-field comparison shows differences on the order of 10% in the sub-mJy region. At these fluxes there are of order 10,000 galaxies per field (Figure 3) so that counting statistics can account for only a fraction of this difference. Even more striking is the large variations in the vicinity of 3 mJy. Taken together, these differences are almost certainly due to sample variance, significant even on 3 degree scales.

Total SWIRE counts were computed from the combined sample with corrections for incompleteness applied. Uncertainties in the counts were estimated using a bootstrap technique, in which samples of identical size to the original are drawn with replacement from the total sample. The standard deviation of the counts derived from the bootstrap samples provides the error bars. The uncertainties are generally quite similar to what is expected from Poisson statistics, but are somewhat larger at higher flux levels. Since the counts are derived from six widely spaced fields, sample variance effects should be averaged out. The total SWIRE counts are shown in Figure 5 and are tabulated in Table 2.

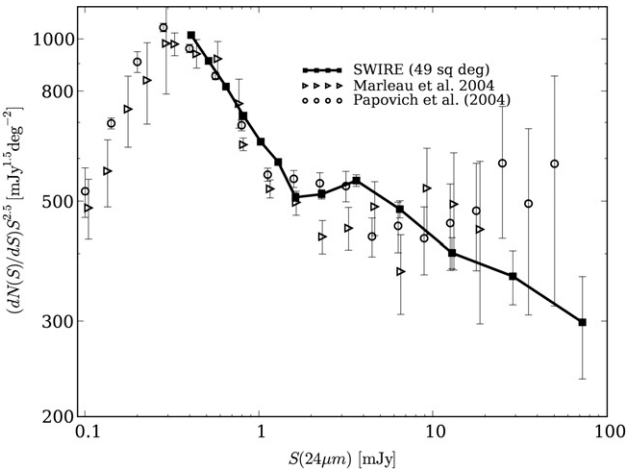

Figure 5. Plot of normalized number counts from the average of all SWIRE fields, along with those of Papovich et al. (2004) and Marleau et al. (2004).

Table 2
Total SWIRE 24 μm Counts

Average F_ν (mJy)	Normalized Counts (mJy$^{1.5}$ deg^{-2})	Uncertainty (mJy$^{1.5}$ deg^{-2})
0.405	1018.81	4.93
0.510	912.33	5.34
0.642	817.73	6.15
0.809	722.46	6.82
1.018	645.91	7.81
1.282	592.51	8.97
1.613	509.69	9.08
2.279	516.15	10.21
3.612	547.15	13.38
6.423	484.33	17.76
12.816	402.43	26.17
28.691	364.24	41.77
72.069	299.29	64.37

We have also plotted the counts for the FLS (Marleau et al. 2004) and GTO fields (Papovich et al. 2004) for comparison. To put the Papovich counts on the SWIRE calibration, we multiplied the fluxes from that work by a factor of 1.059 to account for our color correction, the change in calibration factor (MIPS Data Handbook 2006), and a very slight difference in aperture corrections. The FLS counts were shifted assuming a flux scale fainter than ours by a factor of 1.11, due to the color correction, the change in calibration factor, and our 5% larger aperture correction for a 30.5″ diameter aperture. The steep rise in the normalized counts found by these works is confirmed by our results. There are some differences at brighter flux levels, but these appear to be within the range of the SWIRE field-to-field variations shown by the error bars. Also of note is a "shoulder" at about 3 mJy, seen in the total SWIRE and Papovich et al. (2004) counts, though not in the Marleau et al. (2004) counts, and also not in the ELAIS S1 counts (Figure 4).

4. COMPARISON OF COUNTS WITH MODELS

A plot of the normalized counts with several models overlaid is in Figure 6. The counts used include the SWIRE counts, the Papovich et al. (2004) counts at fainter fluxes, and *IRAS* counts from the sample of Shupe et al. (1998) corrected to the mean MIPS wavelength of 23.7 μm. The fitting of several pre-*Spitzer*-launch models have already been discussed in

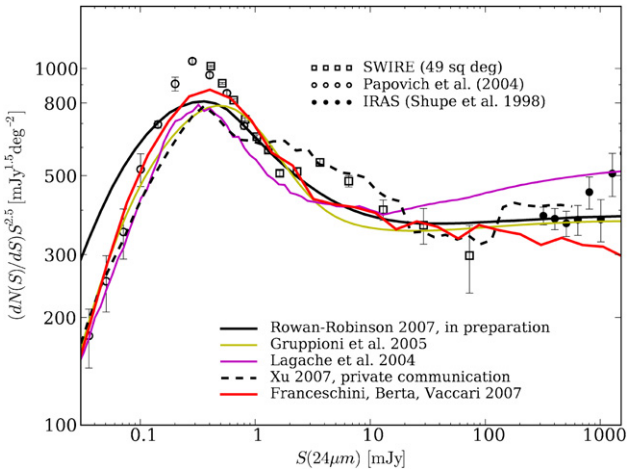

Figure 6. Plot of normalized number counts with several models overlaid.

Chary et al. (2004) and Papovich et al. (2004). Here we focus on more recently available models. One of these models is described in detail in Lagache et al. (2004) and is not outlined here. We give a thumbnail sketch of the other models in turn.

4.1. Details on Individual Models

The Gruppioni et al. (2005) model is based on starburst+cirrus galaxies from Pozzi et al. (2004) and active galactic nucleus (AGN) components from Matute et al. (2006). These works are 15 μm models based on data from the ELAIS survey (Rowan-Robinson et al. 2004). They have been converted to 24 μm using the appropriate ratio of 24 μm–15 μm of each population. Though this work was published after the launch of *Spitzer*, it did not involve an *a posteriori* correction.

The predicted 24 μm counts by Franceschini et al. (2007, in preparation) are based on an IR multi-wavelength evolutionary model (Berta 2005, 2006) fitting a variety of data from *Spitzer*, the *Infrared Space Observatory* (*ISO*), SCUBA, and reproducing data on the diffuse far-IR background observed by *COBE*. The model basically adopts, in addition to normal spiral galaxies and type-1 quasars, two populations of starbursting galaxies with different luminosity functions and evolution rates. One population consists of moderate-luminosity starbursts with peak activity at $z \sim 1$ (the LIRG population), the second contains more luminous objects (the ULIRG and HYLIRG) with maximum activity phase at $z \sim 2$. This evolutionary bimodality is apparently required for a combined fit of the multi-wavelength counts and redshift distributions.

The Xu et al. (2007, private communication) model includes a new evolution model for dusty galaxies and the E2 model for the E/S0s evolution (Xu et al. 2003). The new dusty galaxy evolution model is a modified version of model S1, the starburst-dominant model, in Xu et al. (2003). The definitions of galaxy populations (starbursts, normal disks and AGNs) are the same as in model S1, as are the evolution parameters of the normal disks and AGNs. Both the luminosity evolution rate and density evolution rate of the starburst galaxies are on the order of $(1+z)^3$ for $z \lesssim 1$ and $(1+z)^{-1.5}$ for larger redshifts. The major changes are in the SEDs of the starbursts and normal disks: for both populations the strength of the PAH features in the wavelength range of 5 μm $< \lambda <$ 12 μm is raised by a factor of 2.

The model of Rowan-Robinson et al. (2007, in preparation) is a modification of the counts model of Rowan-Robinson (2001). It retains the four infrared SED types of the latter, with no modification of the SEDs (unlike the new models of Lagache et al. 2004; Xu et al. 2007, private communication). The four types still all undergo strong luminosity evolution but the evolution is allowed to be at a different rate in the different components. The evolution of the cirrus (quiescent) component is now shallower than the evolution of the M82 starburst component, and is considerably steeper for the Arp 220 (high optical depth starburst) component. The evolution function is also modified so that the evolution is less steep at $z < 0.5$ (as in the Lagache et al. 2004 model). The stronger evolution in the Arp 220 component makes the model similar to those of Franceschini et al. (1997), Xu et al. (1998), and Dole et al. (2003), but it still has the distinct feature of strong evolution even in the quiescent component.

4.2. Comments on Model Fits

It is difficult to fit a steep bump in the normalized counts without restricting the luminosities in the models to a narrow range. That said, the models are successful in peaking at about the same flux level (0.3 mJy) as the source counts. The counts rise rather more steeply with decreasing flux, however, so that they peak with counts about 25% higher than the models predict. Some of this difference is due to the color correction and calibration changes applied to the counts, which increase flux by about 5.9% for the (Papovich et al. 2004) counts, and increase normalized counts by about 13%. The model curves could be scaled up by this factor, but in many cases would overpredict brighter sources.

Models which allow evolution of only the more luminous sources, including the possibility of discontinuous changes in the evolution rate, or large changes to source SEDs, have less difficulty in fitting the counts. By contrast, models which use smoothly changing evolution rates, such as those of Rowan-Robinson (2001) and Rowan-Robinson et al. (2007, in preparation), have more difficulty. It is important to establish what really is needed to account for the observed counts. It may be that PAH emission and silicate absorption features at $z \sim 2$ (Houck et al. 2005), or even silicate emission from AGNs (Hao et al. 2005), are stronger or play a larger role than is assumed by the models.

5. COMPOSITION OF 24 μm COUNTS IN ELAIS N1

We now turn to an investigation of the composition of the 24 μm counts. Here we rely on the full optical and *Spitzer*–IRAC data available in the ELAIS N1 field.

5.1. Optical Identifications, Photometric Redshifts, and Infrared Template Fits

We have associated our band-merged N1 catalog, which contains all 24 μm detections with a 3.6 μm counterpart to ensure high reliability, with the optical UgriZ catalog generated from the INT WFS data by Babbedge et al. (2006), using a search radius of 1.5 arcsec. This search radius is appropriate for SWIRE sources detected at 3.6 μm (Rowan-Robinson et al. 2005). The proportions of 24 μm blank fields with confirmed detections in the first two IRAC bands, and with 24 μm flux densities brighter than 200, 300, and 1000 μJy, are 28%, 21%, and 4% respectively, to the WFS survey limit of

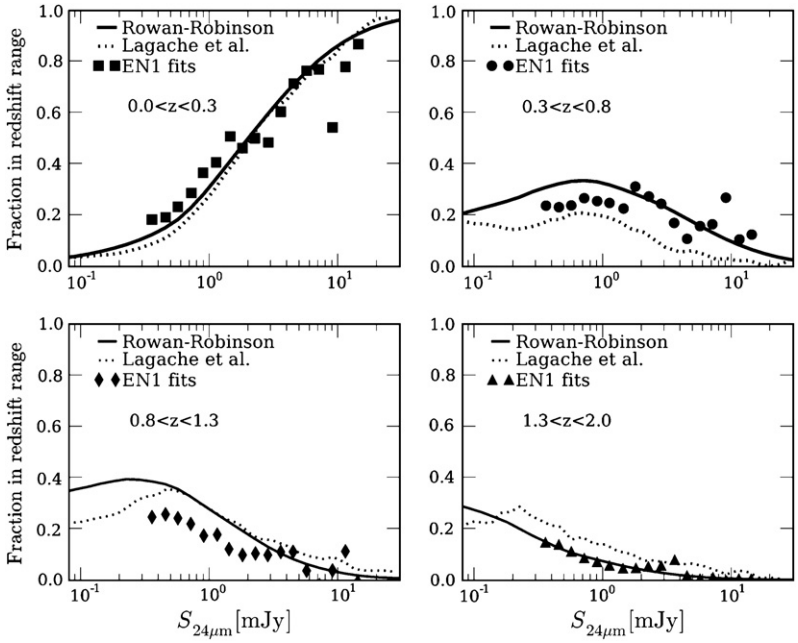

Figure 7. Differential counts fraction at 24 μm subdivided by photometric redshift for the template fits in the SWIRE ELAIS N1 field. The solid and dashed lines are derived from the models of Rowan-Robinson et al. (2008) and Lagache et al. (2004) respectively.

$r \sim 23.5$. For comparison, Babbedge et al. (2006) find that 25% of confirmed SWIRE IRAC sources have optical associations.

All sources with optical associations have been run through the photometric redshift code of Rowan-Robinson (2003) and Babbedge et al. (2004), with small modifications to the SEDs described by Rowan-Robinson et al. (2005, 2008). 20% of 24 μm sources brighter than 200 μJy with optical associations failed to get a photometric redshift because there are less than four bands detected at UgriZ, 3.6, 4.5 μm or because the reduced χ^2 is too poor (>10). This can be because of erroneous optical photometry, incorrect optical associations, or because the range of optical templates used fails to characterize all sources. The latter possibility is worth further study, especially since, for example, strongly reddened quasars or galaxy+quasar combined SEDs are not included in the SED library.

Finally, the SEDs of all 24 μm sources with photometric redshifts are fitted with infrared templates added to the optical/near-IR galaxy and quasar template used in the photometric redshift fit, provided there is an excess in at least two bands relative to the optical/near-IR galaxy model. The templates used are those of Rowan-Robinson et al. (2004), also used earlier in Rowan-Robinson (2001): cirrus, Arp 220 starburst and a mixture of M82 starburst and AGN dust torus. Examples of SED fits using these templates are given by Rowan-Robinson et al. (2005). For sources with an infrared excess only at 24 μm, for which we cannot at this stage characterize the far infrared SED, we have fitted an M82 starburst template. Photometric redshift distributions of 24 μm sources are shown in Rowan-Robinson et al. (2005).

5.2. 24 μm Counts Subdivided by Redshift and Infrared Template Type

The results of the template fitting may be used to break down the infrared counts by redshift range and type. The fraction of counts per redshift range is shown in Figure 7.

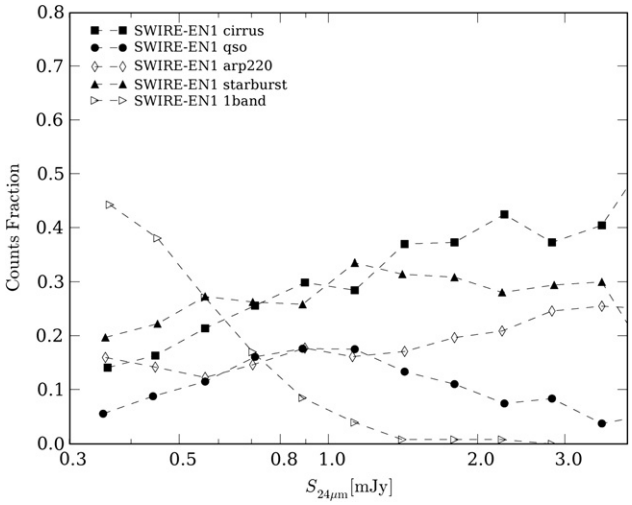

Figure 8. Differential counts fraction at 24 μm subdivided by infrared template type, for the template fitting of SWIRE ELAIS N1 sources.

A related plot is shown in Figure 2 of Babbedge et al. (2006) but here we show the results as a fraction of total counts. Overlaid are the same fractions taken from the models of Lagache et al. (2004) and Rowan-Robinson et al. (2007, in preparation). The template fits and the model are generally in agreement for $z \leqslant 0.3$. The model yields a higher fraction in the higher-redshift bins than the template fits; however since some ELAIS N1 sources did not receive a redshift in the fitting procedure, this may explain the difference. Similar results were found by Le Floc'h et al. (2007, in preparation) and Pérez-González et al. (2005) in which the models generally underpredicted the sources in the low-redshift bins and overpredicted the number at higher redshifts.

Figure 8 shows the 24 μm differential counts subdivided by an infrared template type. We see that the steep rise between

1 mJy and 300 μJy is caused primarily by starbursts, and sources with a infrared excess at 24 μm only. To really understand the 24 μm counts, we need 70 μm data for the sources with infrared excess over the fitted template at 24 μm only. The fraction of sources with quasar-like infrared SEDs is below about 30% at bright fluxes, decreasing to less than 15% at relatively faint fluxes.

6. SUMMARY

The variation between fields of the SWIRE 24 μm number counts shows the importance of sample variance. For fluxes near a few mJy, the field-to-field variation in the counts is 50% to 100% larger than is accountable solely from Poisson uncertainties. Based on redshift estimates from template fitting and from models, the counts variations near 3 mJy may result from large-scale structures around $z \sim 0.5$. At fainter flux levels, the SWIRE 24 μm catalogs will be useful for tracing structures at $z \sim 1$ and beyond.

The 24 μm counts seem exceptionally interesting and most models published before the launch of *Spitzer* miss badly. There may be new populations—Rowan-Robinson et al. (2005) claim there is a large population of Type 2 AGNs that have not been accounted for in previous models. The SWIRE counts confirm a steep rise in the counts from about 2 to 0.3 mJy that is quite difficult for models to fit.

Template fitting to the SWIRE EN1 sources is successful for at least 85% of the galaxies. The photometric redshifts indicate that at least a quarter of the sources in the 1–10 mJy interval have photometric redshifts in the range 0.3–0.8.

The 25 μm band onboard *IRAS* is closest in wavelength space to the MIPS 24 μm passband. *IRAS* counts are complete to about 250 mJy (Shupe et al. 1998) and the SWIRE counts go to about 1000$\times$ fainter. SWIRE results should be the best 24 μm counts above 250 μJy because it will cover the most area of the *Spitzer* extragalactic surveys. The full area of *Spitzer* surveys solidifies the counts up to about 30 mJy, almost allowing linking up with the all-sky *IRAS* counts, but leaving a gap of a factor of 10 in flux. It will be left for the *Akari (ASTRO-F)* and *WISE* missions to bridge this gap.

We are grateful to the referees for their comments, which have led to substantial improvement of this paper. This work is based on observations made with the Spitzer Space Telescope, which is operated by the Jet Propulsion Laboratory, California Institute of Technology under a contract with NASA. Support for this work was provided by NASA through an award issued by JPL/Caltech. SB was supported by a Fondazione Ing. Aldo Gini 2006 grant.

REFERENCES

Babbedge, T. S. R., et al. 2004, MNRAS, 253, 654
Babbedge, T. S. R., et al. 2006, MNRAS, 370, 1159
Berta, S. 2005, Ph.D. thesis, Univ. of Padua
Berta, S. 2006, PASP, 118, 754
Bertin, E., & Arnout, S. 1996, A&A, 117, 393
Chary, R., et al. 2004, ApJS, 154, 80
Dole, H., Lagache, G., & Puget, J.-L. 2003, ApJ, 585, 617
Elbaz, D., Cesarsky, C. J., Chanial, P., Aussel, H., Franceschini, A., Fadda, D., & Chary, R. R. 2002, A&A, 384, 848
Elbaz, D., et al. 1999, A&A, 351, L37
Farrah, D., et al. 2006, ApJ, 641, 117
Franceschini, A., et al. 1997, The Far Infrared and Submillimetre Universe, ESA SP-401, ed. A. Wilson (Noordwijk: ESA), 159
Franceschini, A., et al. 2001, A&A, 378, 1
Gregorich, D. T., Neugebauer, G., Soifer, B. T., Gunn, J. E., & Herter, T. L. 1995, AJ, 110, 259
Gruppioni, C., Pozzi, F., Lari, C., Oliver, S., & Rodighiero, G. 2005, ApJ, 318, 9
Hacking, P., Houck, J. R., & Condon, J. J. 1987, AJ, 316, 15
Hao, L., et al. 2005, ApJ, 625, L75
Houck, J. R., et al. 2005, ApJ, 622, L105
Kron, R. G. 1980, ApJS, 43, 305
Lagache, G., et al. 2004, ApJS, 154, 112
Le Floc'h, E., et al. 2005, ApJ, 632, 169
Lonsdale, C. J., & Chokshi, A. 1993, AJ, 105, 1333
Lonsdale, C. J., et al. 2003, PASP, 115, 897
Lonsdale, C. J., et al. 2004, ApJS, 154, 54
Makovoz, D., & Marleau, F. 2005, PASP, 117, 1113
Marleau, F., et al. 2004, ApJS, 154, 66
Matute, I. La, Franca, F., Pozzi, F., Gruppioni, C., Lari, C., & Zamorani, G. 2006, A&A, 451, 443
MIPS Data Handbook, version 3.2, 2006 February 6, http://ssc.spitzer.caltech.edu/mips/dh/mipsdatahandbook3.2.pdf
Papovich, C., et al. 2004, ApJS, 154, 70
Pérez-González, P. G., et al. 2005, ApJ, 630, 82
Pozzi, F., et al. 2004, ApJ, 609, 122
Rieke, G., et al. 2004, ApJS, 154, 25
Rodighiero, G., et al. 2006, MNRAS, 371, 1891
Rowan-Robinson, M. 2001, ApJ, 549, 745
Rowan-Robinson, M. 2003, MNRAS, 345, 819
Rowan-Robinson, M., et al. 2004, MNRAS, 351, 1290
Rowan-Robinson, M., et al. 2005, AJ, 129, 1183
Rowan-Robinson, M., et al. 2008, MNRAS, submitted
Skrutskie, M. F., et al. 2006, AJ, 131, 1163
Shupe, D. L., Fang, F., Hacking, P. B., & Huchra, J. P. 1998, ApJ, 501, 597
Vaccari, M., et al. 2005, MNRAS, 358, 397
Xu, C., et al. 1998, ApJ, 508, 576
Xu, C. K., Lonsdale, C. J., Shupe, D. L., Franceschini, A., Martin, C., & Schiminovich, D. 2003, ApJ, 587, 90